Preferential orientations of FeRh nanomagnets deposited on a BaTiO_3 epitaxial thin film

A. Reyes, G. Herrera, Pierre Capiod, D. Le Roy, V. Dupuis, I. Cañero-Infante, Guillaume Saint-Girons, R. Bachelet, A. Resta, Philippe Ohresser, et al.

Preferential orientations of FeRh nanomagnets deposited on a $BaTiO_3$ epitaxial thin film

A. Reyes,[1,2] G. Herrera,[1] P. Capiod,[1] D. Le Roy,[1] V. Dupuis,[1] I. Cañero-Infante,[3] G. Saint-Girons,[3] R. Bachelet,[3] A. Resta,[4] P. Ohresser,[4] L. Martinelli,[5] X. Weng,[5,6] G. Renaud,[6] and F. Tournus[1,*]

[1]*Université de Lyon, Université Claude Bernard Lyon 1, CNRS, Institut Lumière Matière, F-69622, Villeurbanne, France*
[2]*Faculty of Sciences, Universidad Autonoma del Estado de Mexico, 50200 Toluca de Lerdo, Mexico*
[3]*Institut des Nanotechnologies de Lyon, CNRS ECL INSA UCBL CPE, F-69621 Villeurbanne, France*
[4]*Synchrotron SOLEIL, L'orme des merisiers, F-91190 Saint-Aubin, France*
[5]*Institut Néel, CNRS-UGA UPR2940, F-38042 Grenoble, France*
[6]*Université Grenoble Alpes, CEA, IRIG-MEM, F-38054 Grenoble, France*

(Received 27 February 2024; accepted 13 May 2024; published 10 June 2024; corrected 14 June 2024)

Size-selected FeRh clusters have been deposited at low energy and under ultra-high vacuum conditions, on a $BaTiO_3$ epitaxial thin film. Using x-ray diffraction in grazing incidence configuration, we have observed the chemical ordering of FeRh nanoparticles into the chemically ordered B2 phase after annealing, while a reciprocal space mapping indicates that particles, despite their random deposition, are finally adopting preferential orientations reflecting an atomic ordering with the $BaTiO_3$ crystal. In addition to the usual epitaxy relationship observed for FeRh thin films, an unexpected orientation is detected (45° in-plane rotation, leading to a new cube-on-cube epitaxy relationship), which must be specific to nanosized FeRh particles.

DOI: 10.1103/PhysRevB.109.245410

I. INTRODUCTION

The binary FeRh alloy displays a rich phase diagram with both crystal and magnetic order phase transitions [1–4]. For the bulk chemically ordered B2 phase (of CsCl type), a first-order antiferromagnetic-ferromagnetic (AFM-FM) transition occurs near room temperature and is appealing for applications such as heat-assisted magnetic recording, or exchange-spring magnets [5,6]. In addition, the subtle link between structure, electronic and magnetic properties [4,7–9] leads to interesting behaviors like magnetostriction, magnetocaloric effect, and the possibility to control the metamagnetic transition using external parameters (pressure, strain or applied field) [10–13]. At the nanoscale, a strong interplay between surface configuration, morphology and magnetic state is expected to take place [14–19]. The AFM-FM transition can then be affected and controlled, by strain or electric field, through the use of a specific substrate [12,13,18,20–27]. Recently, most of the studies were focused on the structure and magnetic properties of FeRh films in presence of interfaces with substrate and overlayer [28–35]. In particular, by using thin films of FeRh grown on monocrystalline surfaces such as MgO and perovskites [9,13,21,25,36–43], it has been shown that the stress between film and substrate strongly affects the transition temperature and the steepness of the metamagnetic transition. On the other hand, little is known about the strain effects on FeRh nanoparticles and their interaction with the surrounding [44–46], while some specific finite size effects have already been reported for these nanomagnets [47–51]. In view to extend to small nanoparticles the successful coupling observed for thin FeRh films grown on ferroelectric $BaTiO_3$ (BTO) substrate [20,39,41], a first step is to investigate the structural properties of FeRh nanoparticles on an epitaxial BTO thin film, to evaluate how far the interface between the nanomagnets and the oxide substrate can be controlled at the atomic level.

In this study, we have deposited size-selected FeRh clusters (diameter lower than 10 nm), at low energy and under ultra-high vacuum (UHV) conditions on BTO thin films. The sample preparation is described in Sec. II. Structural characterization using synchrotron radiation in grazing incidence configuration is reported in Sec. III. We have observed the chemical ordering of FeRh nanoparticles into the B2 phase after annealing. X-ray diffraction indicates that, despite the random deposition of nanoparticles, they are finally adopting preferential orientations, reflecting an atomic ordering with the BTO surface. In addition to the usual epitaxy relationship encountered for thin films, a novel orientation is observed (corresponding to a 45° in-plane rotation). This specific behavior is also obtained for FeRh particles of larger size on a differently prepared BTO film, as shown in Sec. IV, confirming the robustness of these finite size effects. Preliminary magnetic measurements using x-ray magnetic circular dichroism (XMCD) show that the FeRh nanomagnets remain ferromagnetically ordered down to low temperature. This is discussed in Sec. V together with the conclusions and perspectives of this work. These results show how cluster deposition offers an alternative approach to usual bottom-up growth methods and open the path to a possible control of FeRh nanomagnet properties taking advantage of the interfacial coupling, at the atomic level, with a ferroelectric oxide bottom-layer or substrate, notably due to its inherent piezoelectric properties.

*florent.tournus@univ-lyon1.fr

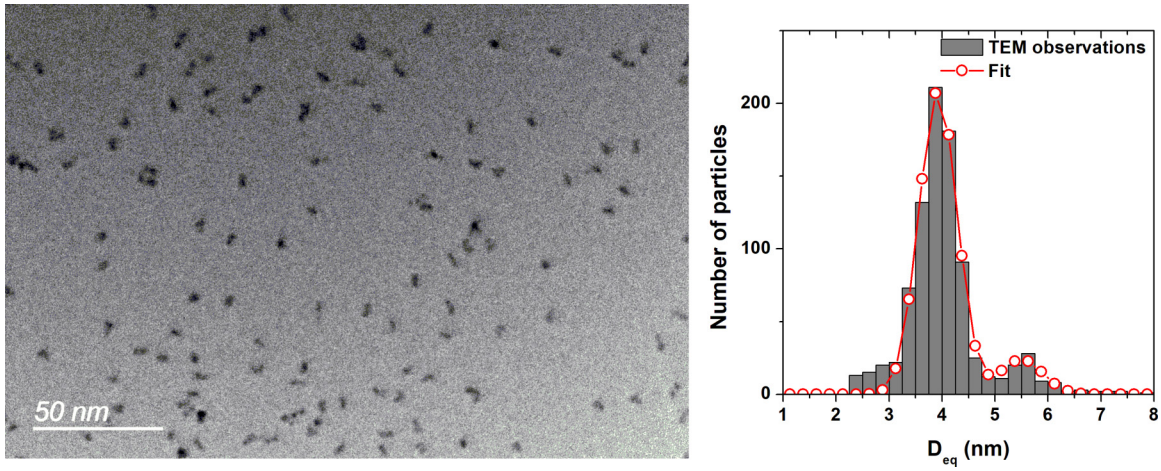

FIG. 1. (Left) TEM image of the incident FeRh clusters, deposited here on an amorphous carbon layer. (Right) Size histogram deduced from TEM observations, with a fit using two gaussians (for the main monomer peak and the small dimer peak).

II. SAMPLE PREPARATION

A BTO thin film of 7 nm thickness has been epitaxially grown using Molecular Beam Epitaxy (MBE) on a $SrTiO_3$ (STO) single-crystal (pure STO(001) square substrates of 5 mm × 5 mm and 0.5 mm thickness). The quality of the BTO thin film, like the crystalline quality and roughness of the surface, was followed by reflection high-energy electron diffraction (RHEED)(see Supplemental Material [52]). The BTO thin film has a stoichiometric and atomically flat surface from the RHEED point of view. As shown in Ref. [53] by *in situ* RHEED, while very thin films (< 5 nm) have a in-plane BTO cell parameter close to that of the substrate (3.905 Å), films thicker than 8 nm are almost completely relaxed. X-ray measurements (see Ref. [52] and further section) confirm the crystal quality and the partially relaxed structure of the BTO film ($a_\perp \simeq 4.08$ Å and $a_\parallel \simeq 3.96$ Å). This partial relaxation is in line with the previously reported x-ray diffraction characterization [54] on the same type of thin films. The BTO diffraction peaks are very close to the STO peaks, the orientation of the thin film corresponds to the STO substrates (001) orientation with a coherent and very small thickness of the layer, indicating a good epitaxial cube-on-cube relationship between the two perovskites. The grown thin film can thus be considered as single crystalline and epitaxial, *c*-domain oriented, the "vertical" direction (i.e., normal to the surface) corresponding to $[001]_{BTO}$.

The FeRh nanoparticles have been synthesized by the mass-selected low energy cluster beam deposition (MS-LECBD) technique [55–58]. Briefly, the plasma created by the incidence of a Nd:YAG pulsed-laser beam focused on an equiatomic FeRh rod is thermalized through the continuous injection of He gas at 30 mbar that induces the nucleation and growth of a cluster beam. Size selection is possible thanks to a quadrupolar electrostatic mass-deviator [59] acting on ionized species that are transferred for deposition in an UHV chamber (10^{-10} mbar base pressure). By using a deviation voltage of 300 V, FeRh clusters pre-formed in the gas phase are deposited at low kinetic energy onto a BTO/STO monocrystalline substrate, at room temperature, with a surface density of around 9×10^3 FeRh clusters/μm^2 (with such a random deposition, the average nearest neighbor distance is then around 5–6 nm, so that around 80% of the incident particles should remain monomers [60,61]). The sample was then coated by a thin amorphous-carbon layer to protect against oxidation and avoid particle diffusion and coalescence [55,56]. A similar sample (with a lower surface density) was also deposited on a transmission electron microscopy (TEM) grid, in order to determine the particle size and shape from TEM observation (see Fig. 1). The FeRh nanoparticles have a mean diameter around 4 nm and the size distribution has a relative dispersion lower than 10% [62]. The total amount of FeRh on the BTO sample is thus of the order of 2 Å, when expressed as an equivalent thickness.

Afterwards, the sample (C/FeRh/BTO/STO) was transferred to the UHV chamber of BM32 beamline of ESRF synchrotron (Grenoble, France) for x-ray diffraction and scattering studies using a 15 keV monochromatized incident beam at grazing incidence. Annealing overnight at 600 °C was performed, in order to reach the chemically ordered B2 phase of FeRh. Such a procedure has been shown (from HRTEM observations, but also synchrotron characterizations [47]) to successfully provide well crystallized FeRh particles when they are embedded in an amorphous carbon matrix. It must be noted that only moderate coalescence and particle size increase is occurring upon annealing, which allows the particles to reach their equilibrium shape and increase the crystalline quality.

III. X-RAY DIFFRACTION CHARACTERIZATION

A. Experimental results

As explained above, chemical ordering and particle recrystallisation is obtained by annealing. Grazing incidence small angle x-ray scattering (GISAXS) can be used to characterize the final nanoparticle size and shape on the substrate [63,64]. With a diluted assembly of particles at random positions on the surface, the GISAXS pattern directly reflects the particle form factor. It can thus be checked that the nanoparticle nature of the sample is preserved (i.e., it is not a continuous FeRh film) with a moderate coalescence between particles initially

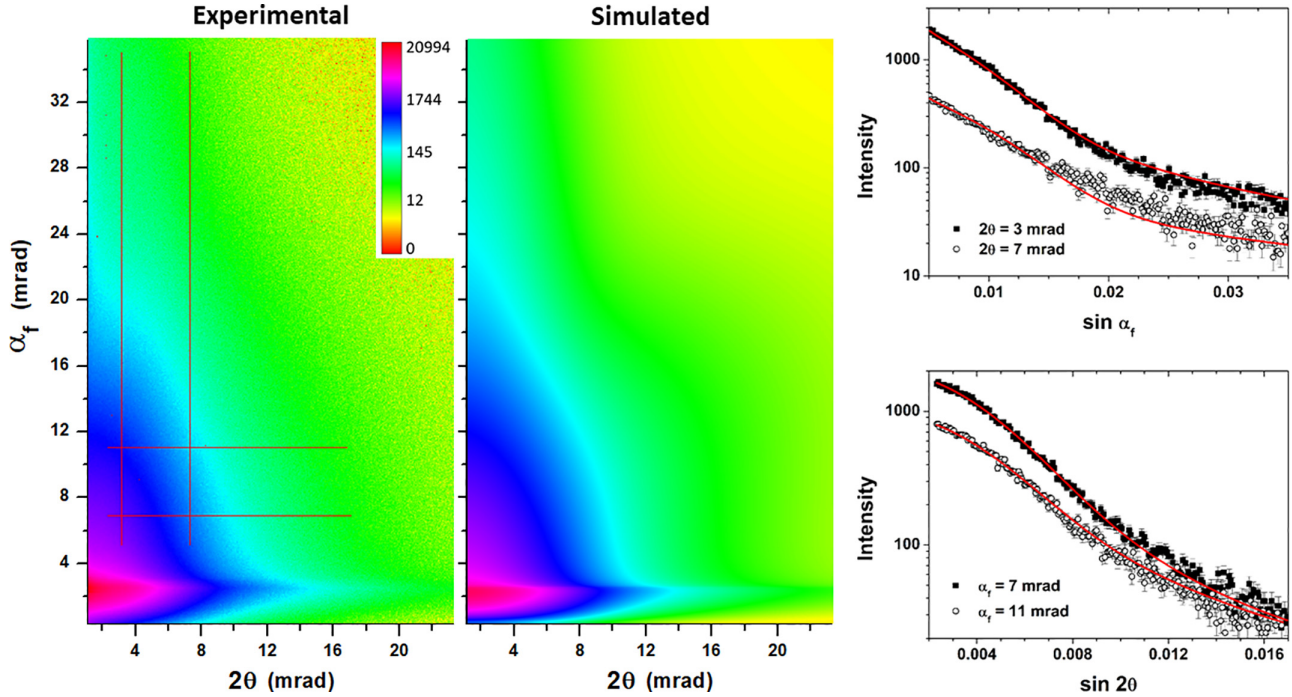

FIG. 2. Experimental GISAXS pattern (left), compared to simulated one (middle), with the 4 sections (right: experimental dots and simulated lines) used to find the best fit parameters (given in text). The 4 sections used are shown as vertical and horizontal lines on the experimental GISAXS pattern.

in contact. The room temperature experimental GISAXS pattern (with an incident angle $\alpha = 0.17^\circ$ close to the critical angle of 0.1365° calculated for BTO) obtained on annealed FeRh sample is compared to a simulated one and presented in Fig. 2. Although the true particle shape and size distribution must be more complex, using the IsGISAXS software [65] a very good fit is obtained with a model assuming hemispheroidal particles of constant flattening parameter ($h/R = 0.93$, with h the particle height and R the in-plane radius) and a simple gaussian distribution for R (centered on $R = 2.83$ nm with a dispersion $\sigma/R = 0.57$). This would correspond to a mean equivalent diameter around 5.6 nm (diameter of a sphere having the same average volume), quite close from the initial particle size. The larger size dispersion may reflect the variety of shapes among the particles which could be less symmetric than ideal hemispheroids (in particular, nanoparticles should rather display facets). Anyway, this shows that the sample still consists of a 2D layer of separate FeRh particles on the BTO surface. The almost perfect hemisphere shape (which gives a much better agreement between simulations and measurements than with spheres, flattened spheres (also called spheroids) or differently truncated spheres [52]) indicates a poor wetting of the oxide surface (90° contact angle), which is the common behavior of metals on oxides. Note however that the particles are more flattened than for metallic clusters on an almost inert graphene surface [64], thus reflecting a non-negligible interaction between FeRh and BTO at the interface. Besides, an in-plane Ω angle variation (i.e., rotation around the normal axis) has no incidence on the GISAXS pattern. This shows that, as far as the particle shape is concerned, there is no orientation effect.

Grazing incidence x-ray diffraction (GIXRD) in-plane scans have been performed before and after thermal treatment. Before annealing, only the BTO and STO peaks were observed (corresponding to crystal truncation rods since we are probing the reciprocal space near the sample surface i.e., $l \simeq 0$ [66]) with no signature of FeRh nanocrystals. This can be explained by the fact that with an initially random orientation of FeRh clusters on the surface, the scattered intensities are spread over and thus diluted on the entire Ewald sphere, making the signal too low to be detected for such small nanocrystals.

After annealing, as shown in Fig. 3, two additional peaks are detected at $q = 2.98$ Å^{-1} and $q = 4.22$ Å^{-1}. They correspond to the $\{110\}_{\text{FeRh}}$ and $\{200\}_{\text{FeRh}}$ peaks of the chemically ordered B2 phase of FeRh. Note that no contribution from the chemically disordered FCC phase of FeRh (called A1) can be detected, otherwise one would observe a peak around $q = 3.43$ Å^{-1} originating from the $\{200\}$ reflection of the FCC phase. This is consistent with a full transformation from A1 (as prepared particles) to B2 phase (annealed particles). From the FeRh peak position we can deduce the cell parameter of FeRh nanocrystals, $a = 2.98$ Å (±0.01 Å), which is fully in line with the bulk lattice constant value [3]. In addition, a typical crystallite size can be evaluated using the Scherrer formula [67,68] by measuring the full width at half maximum (FWHM) of the diffraction peaks. It is around 0.8 nm^{-1}, which corresponds to a diameter $D \simeq 9$ nm, both for $\{110\}_{\text{FeRh}}$ and $\{200\}_{\text{FeRh}}$ peaks. It is also the same in particular azimuths ($[h00]_{\text{BTO}}$ and $[hh0]_{\text{BTO}}$) and in an intermediate direction (22.5° Ω rotation away from the $[h00]_{\text{BTO}}$ direction, thus avoiding any peak from the substrate, as it can be seen in

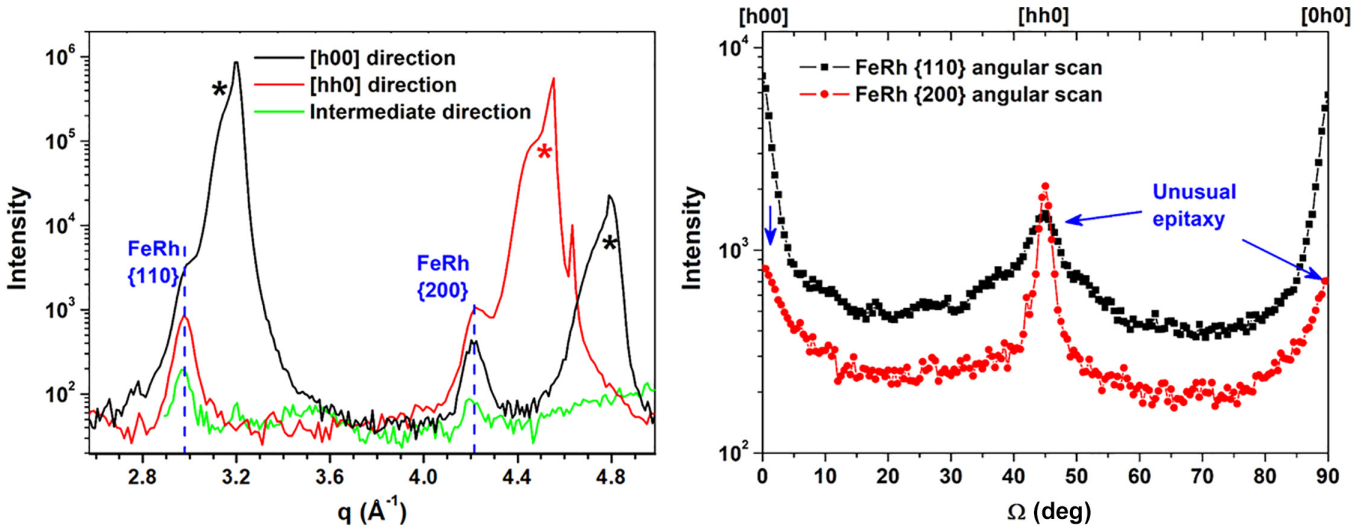

FIG. 3. (Left) GIXRD measurements (radial scans in the reciprocal space, at constant $l \simeq 0$) in logarithmic intensity scale, along different in-plane directions: $[h00]_{\mathrm{BTO}}$, $[hh0]_{\mathrm{BTO}}$, and "intermediate direction" (halfway, i.e., 22.5° away from the two former directions). $\{110\}_{\mathrm{FeRh}}$ and $\{200\}_{\mathrm{FeRh}}$ peaks are visible in addition to substrate peaks marked with stars (STO crystal and BTO thin film, appearing as a shoulder on the left side). (Right) Angular scan, i.e., along different in-plane directions, for the wave vector q corresponding to $\{110\}_{\mathrm{FeRh}}$ and $\{200\}_{\mathrm{FeRh}}$ peaks. The unusual epitaxy results in a higher intensity in particular azimuths of the BTO crystal.

Fig. 3). Note also that since the FWHM is of same magnitude for $\{110\}_{\mathrm{FeRh}}$ and $\{200\}_{\mathrm{FeRh}}$ peaks, the so called "disorder of the second kind" (cell parameter variation) is not apparent and the peak width reflects the finite size on FeRh nanocrystals.

As it is obvious from Fig. 3, the intensity of FeRh peaks strongly varies with the in-plane direction. This means that the particles are neither randomly oriented on the surface (like a powder) nor with a common vertical direction and a random in-plane angle (fiber texture). Remarkably, the intensity ratio between the two azimuths is reversed when we compare $\{110\}_{\mathrm{FeRh}}$ and $\{200\}_{\mathrm{FeRh}}$ peaks. As it has been shown in many experiments [20,23,25,39–41], there exists an usual epitaxy relationship between FeRh and BTO (or STO) encountered for thin films, which is $(001)_{\mathrm{FeRh}} \parallel (001)_{\mathrm{BTO}}$ and $[110]_{\mathrm{FeRh}} \parallel [100]_{\mathrm{BTO}}$. This epitaxy, corresponding to a cube-on-cube stacking with a 45° in-plane rotation between the FeRh and BTO unit cells, is the one called OR II in the review of Fu and Wagner on the interaction of nanostructured metal overlayers with oxide surfaces [69]. According to Fu and Wagner it is the most favorable epitaxy relationship for BCC metals on STO, and it is also observed for thin films of FeRh on BTO or MgO, and for FeRh nanoislands on MgO [29,42,51]. Thus we can expect to observe the same orientation for FeRh nanoparticles lying on a BTO(001) surface: this would be visible with a $\{110\}_{\mathrm{FeRh}}$ peak in the $[h00]_{\mathrm{BTO}}$ direction and the corresponding $\{200\}_{\mathrm{FeRh}}$ peak along the $[hh0]_{\mathrm{BTO}}$ azimuth. Conversely, the signature of the orientation called OR I in the review of Fu and Wagner, which is a direct cube-on-cube stacking (i.e., $(001)_{\mathrm{FeRh}} \parallel (001)_{\mathrm{BTO}}$ and $[100]_{\mathrm{FeRh}} \parallel [100]_{\mathrm{BTO}}$), would be to detect the $\{110\}_{\mathrm{FeRh}}$ peak in the $[hh0]_{\mathrm{BTO}}$ direction and the corresponding $\{200\}_{\mathrm{FeRh}}$ peak along the $[h00]_{\mathrm{BTO}}$ azimuth.

Therefore the GIXRD results can be understood with a mixing of two epitaxy relationships (the usual OR II and the unexpected OR I), corresponding to two different families of FeRh particles on the BTO surface, with $[001]_{\mathrm{FeRh}}$ normal to the surface [70]. Note that the usual epitaxy (cube-on-cube with a 45° rotation) gives the most intense signal, and taking the intensity ratio as a population ratio, we find that the unusual epitaxy (OR I: cube-on-cube) is around 3 times less abundant. However, this is only a crude estimation because there must be additional FeRh particles having neither OR I nor OR II orientation since FeRh peaks are detected in the intermediate direction: therefore, a non negligible proportion of particles may be randomly oriented or with a fiber texture (in-plane random orientation).

To go further, angular scans (also called rocking Ω scans i.e., measurements at a fixed q in-plane, and varying the orientation with a Ω angle sweep) have been measured (see Fig. 3, right) and corroborate the above interpretation in terms of two families of FeRh particles in epitaxy with the BTO substrate. The curves display maximum of intensity every 45° (corresponding to $\langle h00\rangle_{\mathrm{BTO}}$ and $\langle hh0\rangle_{\mathrm{BTO}}$ directions), while a removal of the background signal (including the tail of substrate peaks) rather indicates an intensity ratio between 3 and 4 for the usual epitaxy compared to the unusual one [52]. The reciprocal space map of the surface has also been measured [71], at the SIXS beamline of SOLEIL synchrotron (St Aubin, France), as shown in Fig. 4. In addition to some ring structures (signature of randomly oriented particles), it is clear that along particular azimuths (of $\langle h00\rangle_{\mathrm{BTO}}$ and $\langle hh0\rangle_{\mathrm{BTO}}$ type) we observe a higher intensity both for $\{110\}_{\mathrm{FeRh}}$ and $\{200\}_{\mathrm{FeRh}}$ peaks. Note that for the usual epitaxy (OR II), the FeRh peaks are situated just before the BTO peaks (i.e., at slightly lower q), while for the unusual epitaxy (OR I), they are situated in a region with no other signal coming from the substrate.

B. Discussion

The B2 phase of FeRh corresponds to a BCC metal with a chemical order (like CsCl) so that nanocrystals should mainly display {100} and {110} facets [49], as already observed for

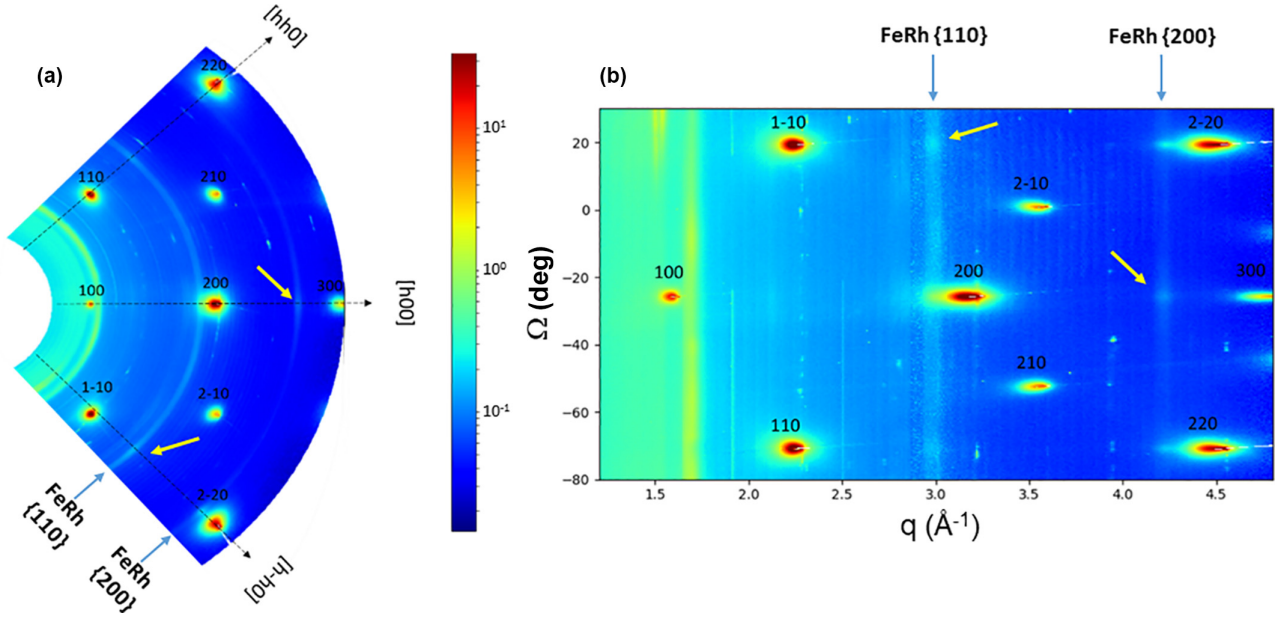

FIG. 4. (Left) Reciprocal space map measured by GIXRD (the color correspond to log scale of the intensity) in a h, k projection ($l \simeq 0$). The main peaks correspond to the substrate. FeRh peaks are detected with higher intensity in particular azimuths (even if a ring structure is visible). (Right) Same map, plotted as a function of q (in-plane wave vector modulus) and Ω angle (rotation around $[001]_{\mathrm{BTO}}$). Therefore a horizontal cut corresponds to a given in-plane direction, while a vertical cut corresponds to a given q. The $\{110\}_{\mathrm{FeRh}}$ peak is situated near $q = 3$ Å^{-1} and the $\{200\}_{\mathrm{FeRh}}$ peak near near $q = 4.2$ Å^{-1}. The higher intensity corresponding to the unusual epitaxy relationship is emphasized by arrows. Substrate peaks appear as elongated on the small-q side due to the partially relaxed epitaxy of the BTO thin film on STO. Note that tails of the substrate {310} peaks are visible on the rightmost part of the map (around 4.7 Å^{-1}).

small particles in amorphous carbon or alumina or grown on MgO [47,49,51]. Even if the interface energy with the BTO(001) surface is not known, it is then reasonable to expect to have FeRh particles with a ⟨001⟩ or ⟨110⟩ direction oriented perpendicular to the surface. It must be noted that particles lying on higher index facets such as {211} or {111} may exist, but they would not result in $\{200\}_{\mathrm{FeRh}}$ peaks observable in the surface plane. Therefore they cannot account for the present observations (moreover, particles on a {111} facet would produce a diffraction pattern with a threefold symmetry, which is not what we see). In addition to the two epitaxy relationships mentioned above, corresponding to FeRh particles lying on a {100} facet with the orientations OR I and OR II according to the list of Fu and Wagner, one may wonder if the two other orientations corresponding to particles on a {110} facet are met in the present case (namely OR III where $[100]_{\mathrm{FeRh}} \parallel [100]_{\mathrm{BTO}}$ and OR IV where $[111]_{\mathrm{FeRh}} \parallel [110]_{\mathrm{BTO}}$). Since OR IV would not result in a strong intensity of $\{110\}_{\mathrm{FeRh}}$ and $\{200\}_{\mathrm{FeRh}}$ peaks along $[h00]_{\mathrm{BTO}}$ and $[hh0]_{\mathrm{BTO}}$ azimuths, contrary to what is observed, this orientation can also be discarded [72]. Finally, if one envisage the existence of FeRh particles having OR III (for instance with $[0\bar{1}1]_{\mathrm{FeRh}}$ perpendicular to the surface and $[100]_{\mathrm{FeRh}} \parallel [100]_{\mathrm{BTO}}$ in plane), then this family of particles would only produce $\{110\}_{\mathrm{FeRh}}$ and $\{200\}_{\mathrm{FeRh}}$ peaks along $\langle h00\rangle_{\mathrm{BTO}}$ azimuths (with a 90° angle between $[200]_{\mathrm{FeRh}}$ and $[011]_{\mathrm{FeRh}}$). The unusual epitaxy relationship OR I is thus the only one able to explain the specific higher intensity observed for $\{110\}_{\mathrm{FeRh}}$ along the $\langle hh0\rangle_{\mathrm{BTO}}$ directions. Because OR III would reinforced the intensity of both $\{110\}_{\mathrm{FeRh}}$ and $\{200\}_{\mathrm{FeRh}}$ in the $\langle h00\rangle_{\mathrm{BTO}}$ azimuths, the observed ratios of intensity mean that particles having this orientation, even if they can exist in principle (this orientation would however be unprecedented for FeRh on perovskite), are in negligible amount. From these considerations, one can deduce that the observed FeRh peaks in the reciprocal space map are due to particles lying on a {100} facet, with some of them displaying the unusual OR I orientation. Although L-scans (i.e., in a direction perpendicular to the surface, corresponding to $[00l]_{\mathrm{BTO}}$) did not give exploitable results, scans at a value $l \neq 0$ have been successfully measured. Remarkably, peaks of FeRh are clearly detected with radial scans (parallel to the surface) at a fixed $l = 1.305$ (in STO relative lattice units), which corresponds to $\{001\}_{\mathrm{FeRh}}$, and along different in-plane directions [52]. This is the signature of FeRh particles lying on a {100} facet, and presenting the same in-plane preferential orientations with respect to the BTO lattice: the $\{110\}_{\mathrm{FeRh}}$ is more intense in the $[hh0]_{\mathrm{BTO}}$ azimuth, since it is situated over the $\{100\}_{\mathrm{FeRh}}$ peak in-plane (i.e., corresponding to the usual OR II epitaxy, being again around 3 times more intense than OR I).

Other FeRh peaks are also of interest. In-plane measurements allow us to detect the (quite weak) {100} peak of FeRh B2, which is directly related to the chemical ordering and which would be absent in the case of a chemically disordered BCC crystal. No peaks corresponding to $\{111\}_{\mathrm{FeRh}}$ or $\{210\}_{\mathrm{FeRh}}$ are detected, which is consistent with their expected very low intensity. On the contrary, the $\{211\}_{\mathrm{FeRh}}$ is expected to be quite intense (for a powder diffraction experiment). It cannot be observed with particles lying on a {100} facet, while for particles on a {110} facet some $\{211\}_{\mathrm{FeRh}}$ peaks appear in the surface plane. Such a peak is observed, with a small intensity (much lower than that of $\{200\}_{\mathrm{FeRh}}$)

comparable in both $[h00]_{\mathrm{BTO}}$ and $[hh0]_{\mathrm{BTO}}$ azimuths and it means that, among the FeRh nanocrystals on the substrate, some of them are not having a {100} facet in contact with the BTO(001) surface. Particles lying on a {110} facet can account for this peak, but many other orientations (that we may call "random" or "disordered") can also produce such a peak. Therefore the ring structure observed for $\{110\}_{\mathrm{FeRh}}$ and $\{200\}_{\mathrm{FeRh}}$ should not be attributed only to a fiber texture (in-plane random orientation of particles lying on a {100} facet) but a background intensity, a priori constant, must also come from other "randomly oriented" FeRh particles.

However, as explained above, the main features in the reciprocal space map of the surface are due to two distinct epitaxy relationships of FeRh nanoparticles presenting a {001} plane in contact with the BTO(001) surface. In particular, the unusual orientation $(001)_{\mathrm{FeRh}} \parallel (001)_{\mathrm{BTO}}$ and $[100]_{\mathrm{FeRh}} \parallel [100]_{\mathrm{BTO}}$ is not observed in the case of thin films grown over BTO or STO. It must nevertheless be noted that a coexistence of this orientation, together with the usual one that we also observe here, was reported for 80 nm thick films deposited by magnetron sputtering on a single crystal of $LaAlO_3$ [40]. The unusual OR I epitaxy for FeRh on BTO thus appears to be specific to the small particle size. The relative abundance (i.e., diffraction peak intensity) of the two families of particles with different epitaxy relationships can reflect the underlying energetic difference between different interfacial atomic configurations, or it can be due to a transition in the most stable state depending on the particle size. This second explanation should not hold in our case, since we do not detect any size difference (from the peak FWHM) for particles of different epitaxies, as well as between "random" particles and those with specific orientations. However, a more precise size-dependence study of this particular behavior would be needed (cf. next section). The FeRh cell parameter, deduced from the peak positions, is also the same for all families of FeRh nanocrystals (OR I, OR II, or random orientation). The observation of a substantial population of particles with OR I must then be ascribed to a small energy difference between this unusual orientation and the usual one.

Even if, as noted by Fu and Wagner, "formation of OR II is also promoted by a high density of near coincident sites for bcc metal atoms on O" and "OR I and OR II are favored by the small misfits," our reciprocal space investigations does not allow us to determine the atomic configuration at the interface corresponding to these two epitaxy relationships. Atomic modeling (with empirical potential or first-principles calculations) could shed light on the underlying physical mechanism but are beyond the scope of the present article. Anyway, for metal/oxide interface Fe atoms usually sit on top of oxygen atoms and Odkhuu *et al.* [18] indeed state from their density functional theory calculations that "the Fe atoms are favored on top of the O sites at the TiO_2 interface." At the nanoscale, it must be kept in mind that relaxation of the FeRh nanocrystals can be significant [19,47] and can play a large role to reach the most favorable configuration. The fact that most of the particles must lie on a {100} facet, while they could also land with a {110} facet on the surface (FeRh clusters present {110} facets when they are embedded in an inert amorphous carbon matrix [47], in agreement with the low surface energy of this kind of facet [19,49]), is the sign of an important particle restructuring at the interface with BTO, permitted by the annealing procedure (thermodynamic equilibrium is *a priori* reached).

The slight shift of the FeRh diffraction peaks with respect to the BTO peaks indicates that the cell parameter of FeRh nanocrystal is not elastically constrained to match the one of the BTO surface. Even if the stacking corresponding to the epitaxy relationship labeled OR II is favorable (cube-on-cube with a 45° rotation), the mismatch between the (real space) interplane spacing d_{110}(FeRh) and d_{200}(BTO) is around 6%. This is quite large and explains that the FeRh nanocrystals display a relaxed in-plane cell parameter: the elastic energy that would be present with a perfectly matching epitaxy can indeed be reduced by defect formation at the interface (such as dislocations) or in the FeRh nanoparticles (stacking faults or twins for instance). The unusual epitaxy labeled OR I is a direct cube-on-cube stacking and, given the respective lattice parameter of FeRh (2.98 Å) and BTO ($a_{\parallel} = 3.99$ Å for the bulk), 4 cells of FeRh almost perfectly correspond to 3 cells of BTO. Therefore, in real space, there is a interplane distance coincidence: $2d_{110}(\mathrm{FeRh}) \simeq 3d_{220}(\mathrm{BTO})$ with a very low mismatch around 0.4%. Note that the situation differs from the reported similar epitaxy of FeRh on $LaAlO_3$ [40] where the substrate cell parameter ($a = 3.792$ Å) is significantly smaller than that of STO (and thus much lower than the 3.99 Å cell parameter of BTO): in the case of such a thin film growth, the unusual cube-on-cube epitaxy corresponds to five FeRh unit cells matching four $LaAlO_3$ unit cells.

The angular width of the FeRh diffraction peaks (measured on the rocking Ω scans) can provide information on the in-plane mosaicity, i.e., the angular spread of the crystal alignment around the nominal epitaxy [73]. We can note that the observed width is significantly larger than the one due to the finite size of FeRh nanocrystals (deduced from the FWHM for radial scans), which would for instance be less than 2° for the $\{110\}_{\mathrm{FeRh}}$ peak. Considering the $\{200\}_{\mathrm{FeRh}}$ peak (similar values are found for $\{110\}_{\mathrm{FeRh}}$), we find that OR II epitaxy has an angular width around 3°–4°, while the signal reflecting OR I has a larger spread of 5°–6° around the $[h00]_{\mathrm{BTO}}$ azimuth. Moreover, the angular profile of the peak does not correspond to a simple gaussian but seems to be made of three different peaks (cf. Fig. 3 and Ref. [52]): broad "satellite" shoulders are found around 6° on both sides of the nominal $[h00]_{\mathrm{BTO}}$ azimuth for OR I epitaxy. Although energetical modeling are needed to get deeper insight, this is an indication that the potential well responsible for the existence of the unusual epitaxy must be wider/softer than for the usual epitaxy relationship.

Such a behavior has already been observed for instance in the case of the compliant growth of InP nanocrystals on STO [74], where despite incommensurability, InP islands are oriented with respect to the STO(001) substrate (with a {111} InP plane at the interface, resulting in a hexagonal symmetry visible on the reciprocal space map). Remarkably, simple calculations with empirical potentials predict a transition of optimal angles for the growth as a function of the extension of the (111) basal plane of InP islands: the same kind of phenomenon could be at play in the present case. A size dependence of epitaxy relationships has also been reported for Pt islands on MgO(001) [73]. For this system, the most

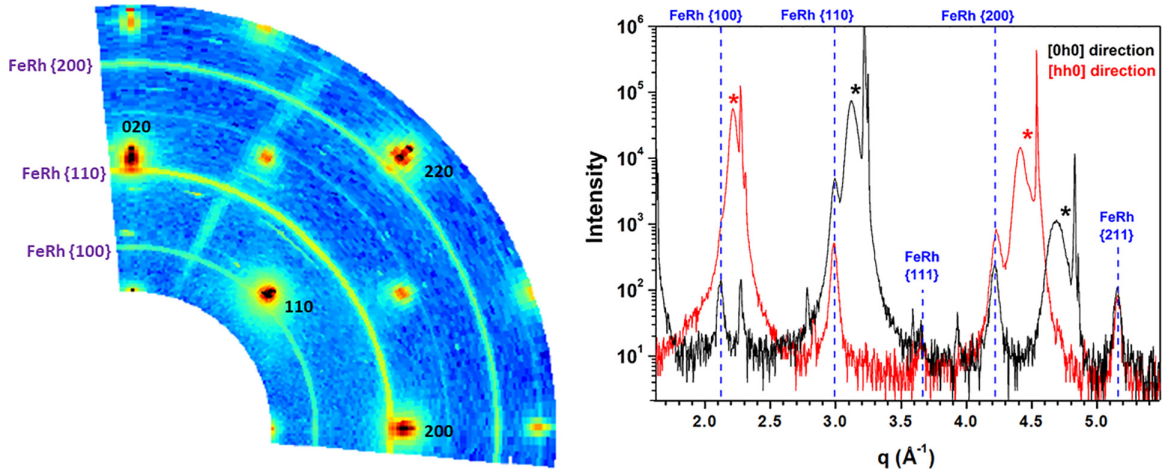

FIG. 5. (Left) Reciprocal space map measured by GIXRD (the color correspond to log scale of the intensity) in a h, k projection ($l \simeq 0$). The main peaks correspond to the substrate. FeRh peaks are detected as rings, with higher intensity in particular azimuths. (Right) GIXRD radial scan in particular directions in the surface plane. Some small parasitic peaks are also visible in addition to the FeRh "ring" signal and to the most intense diffraction peaks of the substrate, marked with a star (STO crystal and relaxed BTO thin film, appearing as a shoulder on the low-q side).

favorable orientation displays a striking transition with the crystal size. In addition, well defined satellite peaks are observed on rocking Ω scans and can be explained by the appearance of size-dependent local minima in the interfacial energy as a function of crystal relative orientations. A similar feature, with secondary preferential orientations giving rise to satellite peaks as a function of island size, has been reported for small model catalysts of Au grown on TiO_2(110) surface [75]. These studies are example of striking finite size effects, resulting in specific behavior at the nanoscale for the epitaxial growth of particles on oxide surfaces. The present study demonstrates that in the case of preformed clusters deposition, even if the situation is in principle different (it is not a growth with islands of progressively increasing size), the same kind of physical mechanisms can be met.

IV. DEPOSITION OF LARGER FeRh PARTICLES

To confirm and extend the investigation to larger size FeRh particles, we have considered a second sample of clusters deposited using a higher deviation potential (1200 V) and thus resulting in a significantly larger nanocrystal diameter. The amount of deposited particles corresponds to an equivalent thickness near 10 Å. Therefore a substantial coalescence (and recrystallisation) is expected between initially touching particles during the annealing step to promote chemical ordering into the B2 phase of FeRh (the sample is capped by amorphous carbon and the procedure is the same as for the preceding sections). The final size distribution is also expected to be wider: it will not be precisely determined but the mean crystal diameter can be evaluated from the diffraction peak width. For this sample, the BTO surface was not grown by MBE but using a radio-frequency sputtering procedure, still on a TiO_2 terminated STO(001) single crystal, resulting in the epitaxy of a continuous thin film of the same thickness (7 nm), relaxed in plane.

The reciprocal space map of the surface (GIXRD measurements at BM32 beamline of ESRF) is shown in Fig. 5, together with some radial scans in different azimuths. All the expected diffraction peaks of FeRh B2 phase are detected, including the low intensity {111} reflection (and a potential faint signal due to the {210} reflection), with no sign of other phases. From the measured FWHM (around 0.35 nm^{-1}) and according to the Scherrer equation, the crystal size is about 20 nm. This is notably larger than for the previous sample. The FeRh peaks intensity is again dependent on the in-plane azimuth with respect to the BTO surface, as it can be seen from the GIXRD map but also from angular scans for wavevectors corresponding to $\{110\}_{\text{FeRh}}$ and $\{200\}_{\text{FeRh}}$. Figure 6 displays the evolution of the intensity of these FeRh peaks (the background contribution from substrate peaks has

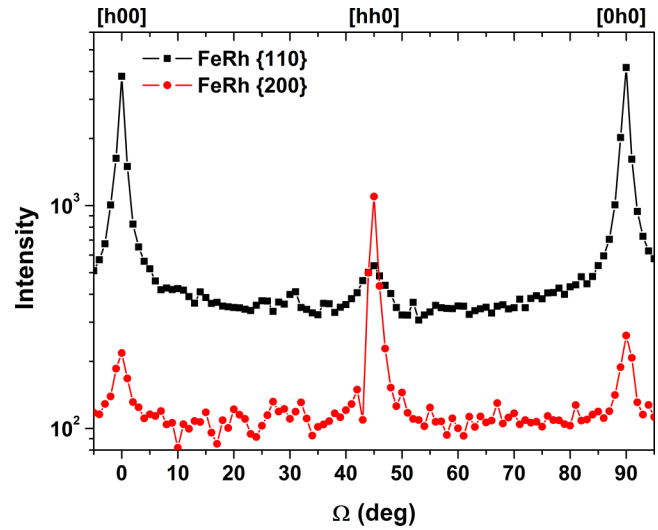

FIG. 6. Intensity of $\{110\}_{\text{FeRh}}$ and $\{200\}_{\text{FeRh}}$ peaks deduced from angular scans, i.e., along different in-plane directions. The background signal coming from the substrate peaks has been subtracted when needed. The higher intensity along particular directions is the signature of preferential orientations (epitaxy relationships).

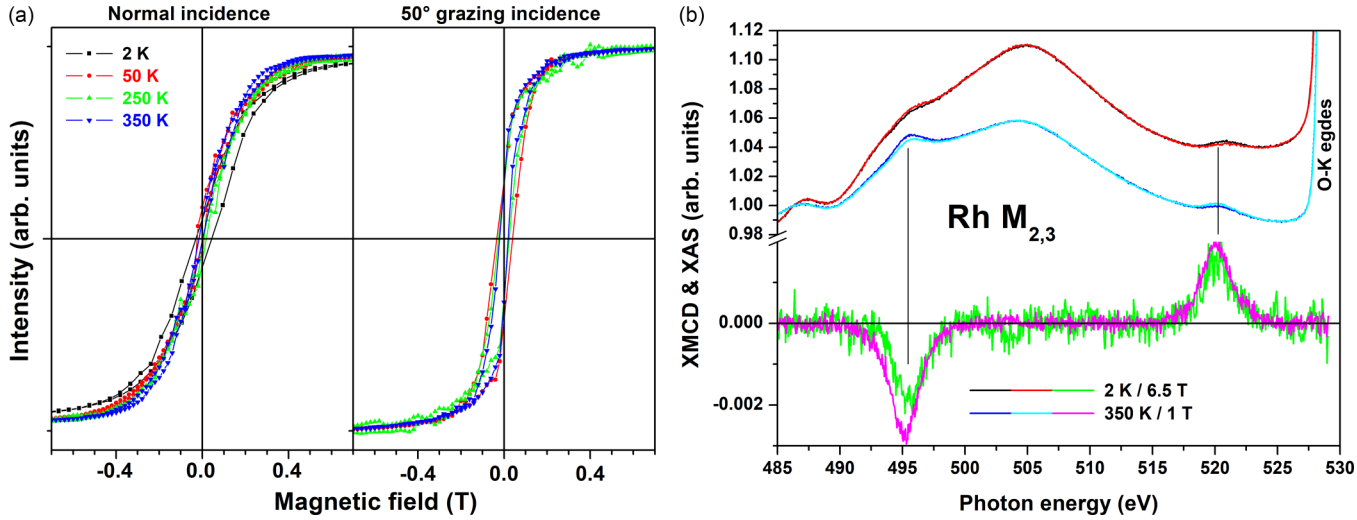

FIG. 7. XMCD measurements on the FeRh particles of Sec. IV. (a) Hysteresis loops measured at the Fe L_3 edge (maximum XMCD signal), for different temperatures, with a normal or grazing incidence of the x-ray beam (and thus a different direction of the applied magnetic field). (b) XAS and XMCD signals at the Rh $M_{2,3}$ edges, at 350 and 2 K for a normal incidence.

been removed) as a function of the in-plane azimuth. While a constant intensity corresponding to randomly oriented FeRh particles is present (ring on the GIXRD surface map), a higher intensity for specific directions is observed, as for smaller FeRh particles: the usual $(001)_{\mathrm{FeRh}} \parallel (001)_{\mathrm{BTO}}$ and $[110]_{\mathrm{FeRh}} \parallel [100]_{\mathrm{BTO}}$ epitaxy relationship (OR II) gives a high intensity of $\{110\}_{\mathrm{FeRh}}$ along $\langle h00\rangle_{\mathrm{BTO}}$ and of $\{200\}_{\mathrm{FeRh}}$ along $\langle hh0\rangle_{\mathrm{BTO}}$, and the unusual (OR I) epitaxy where $(001)_{\mathrm{FeRh}} \parallel (001)_{\mathrm{BTO}}$ and $[100]_{\mathrm{FeRh}} \parallel [100]_{\mathrm{BTO}}$ on the contrary results in a high intensity of $\{110\}_{\mathrm{FeRh}}$ along $\langle hh0\rangle_{\mathrm{BTO}}$ and of $\{200\}_{\mathrm{FeRh}}$ along $\langle h00\rangle_{\mathrm{BTO}}$. Let us insist on the fact that only OR I, which is not met for FeRh thin films on BTO or STO, can account for the latter higher intensity in those particular azimuths. Therefore, even for FeRh nanoparticles of larger diameter, we observe a coexistence of the two epitaxy relationships.

The angular width of particles corresponding to OR I seems a bit larger than that of OR II, although for this sample there is no clear sign of multiple peaks ("satellites"), meaning that the underlying energetic landscape may be different from the previous sample. Another effect of the larger particle size is that the OR II to OR I ratio (between 10 and 15, from a crude estimation of the peak intensity contributions) is significantly higher than previously. Moreover, in the present case, one cannot exclude the presence of particles corresponding to OR III (unprecedented for FeRh grown on STO or BTO), since it would also induce higher intensity of $\{110\}_{\mathrm{FeRh}}$ and $\{200\}_{\mathrm{FeRh}}$ along $\langle h00\rangle_{\mathrm{BTO}}$ directions. It should also be noted that, certainly due to the large amount of deposited particles (some of them could even not be in contact with the BTO surface), a significant signal comes from "randomly oriented" FeRh particles (rings in the map). The rings cannot be only due to particles lying on a {100} facet with a random in-plane orientation, since we also detect {111} and {211} peaks of FeRh which cannot be obtained with such particles.

These measurements demonstrate that the occurrence of the unusual epitaxy relationship (OR I) is a robust feature of the interfacial interaction between FeRh nanoparticles in the B2 phase and a BTO(001) crystal. The observed evolution with particle size, together with the known limit of "infinite size" (i.e., a thick FeRh film) where only the usual OR II is observed, is a manifestation of a specific size effect in this nanosystem.

Since the interface between FeRh particles and the substrate is well-defined, this is a first step to envisage a control of their magnetic properties through the substrate. A major motivation was to possibly modify the metamagnetic transition of FeRh (or to make it exist, because for assemblies of small FeRh particles in a matrix it is still not observed [47,50]), using strain or electric polarization in the perovskite crystal. This is beyond the scope of the present study but preliminary magnetic measurements have been performed at the DEIMOS beamline [76] on the same samples used for GIXRD experiments (after air transfer). Due to the small amount of matter, synchrotron radiation has been used to acquire the x-ray absorption signal (XAS) and the corresponding x-ray magnetic circular dichroism (XMCD) signal at Fe $L_{2,3}$ and Rh $M_{2,3}$ edges. From the shape of Fe L edge, we find that the FeRh particles are significantly oxidized (see Supplemental Material [52]), which may come from an inefficient (porous) capping layer that was used to protect the particles or to oxygen atoms of the substrate. Note that for the similar $Fe/BaTiO_3$ system, it has been shown that at the interface an ultrathin oxidized iron layer exists, whose magnetization can be electrically and reversibly switched on and off at room temperature by reversing the BTO polarization [77].

Anyway, a XMCD signal is visible and we have followed the magnetic response of Fe from 350 K down to 2 K [see Fig. 7(a)]. There is no sign of metamagnetic transition as we always measure a noticeable XMCD signal, even at low temperature. We only observe an opening of the hysteresis loop when the temperature is lowered, which is the expected behavior for ferromagnetic nanoparticles [78]. Note that the hysteresis loops are different for normal and grazing incidence, with an easy in-plane magnetization indicating an overall planar anisotropy that must be due to dipolar interactions (shape anisotropy as for a thin magnetic film). This

can be understood given the large amount of deposited particles in this sample. Nevertheless, additional subtle interface effects on the magnetic anisotropy of the particle can exist [15,16,18,79], but require better controlled samples (i.e., more diluted assemblies of well-defined nanomagnets) to be able to decipher them from other phenomena. Interestingly, precisely thanks to the quite large quantity of FeRh on the surface, it is possible to detect a Rh XMCD signal at the $M_{2,3}$ edge [see Fig. 7(b)] situated just before the oxygen K edge. This magnetic signal, much similar at 350 K and at low T, further confirms that there is no metamagnetic transition taking place in the nanoparticle assembly: the FeRh particles (with a typical 20 nm diameter, according to the GIXRD measurements) remain ferromagnetic, as for small FeRh clusters embedded in amorphous carbon [47]. Additional investigations are needed if we want to detect potential impacts of preferential orientations (especially the unusual epitaxy relationship) on the magnetic properties of FeRh nanomagnets.

V. CONCLUSION

In conclusion, an unconventional epitaxy relationship, $(001)_{\mathrm{FeRh}} \parallel (001)_{\mathrm{BTO}}$ and $[100]_{\mathrm{FeRh}} \parallel [100]_{\mathrm{BTO}}$, has been observed for assemblies of FeRh nanoparticles, deposited under UHV on a BTO thin film grown on STO(001) single crystal, and subsequently annealed to reach thermodynamic equilibrium. The particles have been shown to be crystallized in the chemically ordered B2 phase which, in the case of bulk FeRh or thin films, undergoes a metamagnetic transition (from AFM order to FM order) close to room temperature. The existence of preferential orientations between FeRh nanocrystals on the surface and the BTO substrate is the signature of an intimate contact, at the atomic level, between deposited nanoparticles and the crystal surface. Although the usual epitaxy relationship (cube-on-cube with a 45° rotation) is also seen, and remains the major one, cluster deposition appears as an original and powerful method to produce nanosystems with particular finite size effects. Further theoretical studies would be beneficial to better understand the energy landscape met with nanocrystals of FeRh on oxide surfaces, especially to get insight on the most favorable real-space configurations, as a function of particle size. This is a rich system, where apparently various favorable arrangements can coexist, and it would be worth to extend the investigations to other oxide substrates such as STO or MgO (where the conventional epitaxy of FeRh is observed). From an experimental point of view, even if a compromise between a better control of the particle size (avoiding contact and coalescence between particles) and a strong enough signal is always necessary, one could try in the future to characterize more diluted FeRh nanoparticles assemblies. This will for sure be challenging, but it could reveal subtle size effects and a larger proportion of particles displaying an epitaxy relationship may be achieved. Further magnetic investigations are also planned in the future.

ACKNOWLEDGMENTS

This work has been partly funded by the VOLCONANO project of French ANR (Ref. ANR-19-CE09-0023). The authors would like to acknowledge the "Plateforme LYonnaise de Recherche sur les Agrégats" (PLYRA) of iLMTech for sample preparation, and especially C. Albin and O. Boisron for their technical support. We acknowledge the European Synchrotron Radiation Facility (ESRF) for provision of synchrotron radiation facilities under Proposals No. 20160911 and No. 32-03-745 and we would like to thank the staff of BM32 for assistance and support in using the beamline. We also acknowledge the SOLEIL synchrotron for provision of synchrotron radiation facilities under Proposals No. 20171179, No. 20180150, and No. 99200192 and we would like to thank the staff of SIXS and DEIMOS for assistance and support in using their beamline.

[1] M. Fallot and R. Hocart, Sur l'apparition du ferromagnétisme par élévation de température dans des alliages de fer et de rhodium, Rev. Sci. **77**, 498 (1939).

[2] L. Muldawer and F. deBergevin, Antiferromagnetic-ferromagnetic transformation in FeRh, J. Chem. Phys. **35**, 1904 (1961).

[3] L. J. Swartzendruber, The Fe-Rh (iron-rhodium) system, Bull. Alloy Phase Diagrams **5**, 456 (1984).

[4] V. L. Moruzzi and P. M. Marcus, Antiferromagnetic-ferromagnetic transition in FeRh, Phys. Rev. B **46**, 2864 (1992).

[5] J.-U. Thiele, S. Maat, and E. E. Fullerton, FeRh/FePt exchange spring films for thermally assisted magnetic recording media, Appl. Phys. Lett. **82**, 2859 (2003).

[6] J.-U. Thiele, S. Maat, J. Robertson, and E. Fullerton, Magnetic and structural properties of FePt-FeRh exchange spring films for thermally assisted magnetic recording media, IEEE Trans. Magn. **40**, 2537 (2004).

[7] M. Wolloch, M. E. Gruner, W. Keune, P. Mohn, J. Redinger, F. Hofer, D. Suess, R. Podloucky, J. Landers, S. Salamon, F. Scheibel, D. Spoddig, R. Witte, B. Roldan Cuenya, O. Gutfleisch, M. Y. Hu, J. Zhao, T. Toellner, E. E. Alp, M. Siewert, P. Entel, R. Pentcheva, and H. Wende, Impact of lattice dynamics on the phase stability of metamagnetic FeRh: Bulk and thin films, Phys. Rev. B **94**, 174435 (2016).

[8] N. A. Zarkevich and D. D. Johnson, FeRh ground state and martensitic transformation, Phys. Rev. B **97**, 014202 (2018).

[9] C. Bordel, J. Juraszek, D. W. Cooke, C. Baldasseroni, S. Mankovsky, J. Minár, H. Ebert, S. Moyerman, E. E. Fullerton, and F. Hellman, Fe spin reorientation across the metamagnetic transition in strained FeRh thin films, Phys. Rev. Lett. **109**, 117201 (2012).

[10] E. Stern-Taulats, A. Planes, P. Lloveras, M. Barrio, J.-L. Tamarit, S. Pramanick, S. Majumdar, C. Frontera, and L. Mañosa, Barocaloric and magnetocaloric effects in $Fe_{49}Rh_{51}$, Phys. Rev. B **89**, 214105 (2014).

[11] L. H. Lewis, C. H. Marrows, and S. Langridge, Coupled magnetic, structural, and electronic phase transitions in FeRh, J. Phys. D **49**, 323002 (2016).

[12] K. Qiao, J. Wang, F. Hu, J. Li, C. Zhang, Y. Liu, Z. Yu, Y. Gao, J. Su, F. Shen, H. Zhou, X. Bai, J. Wang, V. Franco, J. Sun, and B. Shen, Regulation of phase transition and magnetocaloric

effect by ferroelectric domains in FeRh/PMN-PT heterojunctions, Acta Mater. **191**, 51 (2020).

[13] X. Zhu, Y. Xu, C. Cao, T. Shang, Y. Xie, and Q. Zhan, Recent developments on the magnetic and electrical transport properties of FeRh- and Rh-based heterostructures, J. Phys.: Condens. Matter **34**, 144004 (2022).

[14] S. Lounis, M. Benakki, and C. Demangeat, Ferromagnetic stabilization of ordered B2 FeRh thin films, Phys. Rev. B **67**, 094432 (2003).

[15] S. Jekal, S. H. Rhim, S. C. Hong, W.-J. Son, and A. B. Shick, Surface-termination-dependent magnetism and strong perpendicular magnetocrystalline anisotropy of an FeRh(001) thin film, Phys. Rev. B **92**, 064410 (2015).

[16] G. Zheng, S.-H. Ke, M. Miao, J. Kim, R. Ramesh, and N. Kioussis, Epitaxial strain controlled magnetocrystalline anisotropy in ultrathin FeRh/MgO bilayers, AIP Adv. **7**, 055914 (2017).

[17] T. A. Ostler, C. Barton, T. Thomson, and G. Hrkac, Modeling the thickness dependence of the magnetic phase transition temperature in thin FeRh films, Phys. Rev. B **95**, 064415 (2017).

[18] D. Odkhuu, Electric control of magnetization reorientation in FeRh/$BaTiO_3$ mediated by a magnetic phase transition, Phys. Rev. B **96**, 134402 (2017).

[19] M. J. Jiménez, A. B. Schvval, and G. F. Cabeza, *Ab initio* study of electronic and magnetic properties of FeRh(001), FeRh(110) and FeRh(111) ultrathin films, J. Magn. Magn. Mater. **526**, 167727 (2021).

[20] R. O. Cherifi, V. Ivanovskaya, L. C. Phillips, A. Zobelli, I. C. Infante, E. Jacquet, V. Garcia, S. Fusil, P. R. Briddon, N. Guiblin, A. Mougin, A. A. Ünal, F. Kronast, S. Valencia, B. Dkhil, A. Barthélémy, and M. Bibes, Electric-field control of magnetic order above room temperature, Nat. Mater. **13**, 345 (2014).

[21] T. Taniyama, Electric-field control of magnetism via strain transfer across ferromagnetic/ferroelectric interfaces, J. Phys.: Condens. Matter **27**, 504001 (2015).

[22] Y. Lee, Z. Q. Liu, J. T. Heron, J. D. Clarkson, J. Hong, C. Ko, M. D. Biegalski, U. Aschauer, S. L. Hsu, M. E. Nowakowski, J. Wu, H. M. Christen, S. Salahuddin, J. B. Bokor, N. A. Spaldin, D. G. Schlom, and R. Ramesh, Large resistivity modulation in mixed-phase metallic systems, Nat. Commun. **6**, 5959 (2015).

[23] L. C. Phillips, R. O. Cherifi, V. Ivanovskaya, A. Zobelli, I. C. Infante, E. Jacquet, N. Guiblin, A. A. Ünal, F. Kronast, B. Dkhil, A. Barthélémy, M. Bibes, and Valencia, Local electrical control of magnetic order and orientation by ferroelastic domain arrangements just above room temperature, Sci. Rep. **5**, 10026 (2015).

[24] G. Zheng, S.-H. Ke, M. Miao, J. Kim, R. Ramesh, and N. Kioussis, Electric field control of magnetization direction across the antiferromagnetic to ferromagnetic transition, Sci. Rep. **7**, 5366 (2017).

[25] A. Ceballos, Z. Chen, O. Schneider, C. Bordel, L.-W. Wang, and F. Hellman, Effect of strain and thickness on the transition temperature of epitaxial FeRh thin-films, Appl. Phys. Lett. **111**, 172401 (2017).

[26] I. Fina, A. Quintana, X. Martí, F. Sánchez, M. Foerster, L. Aballe, J. Sort, and J. Fontcuberta, Reversible and magnetically unassisted voltage-driven switching of magnetization in FeRh/PMN-PT, Appl. Phys. Lett. **113**, 152901 (2018).

[27] Z. Li, J. Zhao, Q. Zhu, X. Lv, C. Cao, X. Zhu, L. Sun, Y. Peng, W. Cheng, D. Jiang, and Q. Zhan, Electric control of magnetic properties in epitaxially grown FeRh/MgO/PMN-PT heterostructures, J. Alloys Compd. **868**, 159220 (2021).

[28] Y. Ding, D. A. Arena, J. Dvorak, M. Ali, C. J. Kinane, C. H. Marrows, B. J. Hickey, and L. H. Lewis, Bulk and near-surface magnetic properties of FeRh thin films, J. Appl. Phys. **103**, 07B515 (2008).

[29] J. Ayoub, C. Gatel, C. Roucau, and M. Casanove, Structure and chemical order in FeRh nanolayers epitaxially grown on MgO(001), J. Cryst. Growth **314**, 336 (2011).

[30] C. Baldasseroni, C. Bordel, A. X. Gray, A. M. Kaiser, F. Kronast, J. Herrero-Albillos, C. M. Schneider, C. S. Fadley, and F. Hellman, Temperature-driven nucleation of ferromagnetic domains in FeRh thin films, Appl. Phys. Lett. **100**, 262401 (2012).

[31] G. C. Han, J. J. Qiu, Q. J. Yap, P. Luo, T. Kanbe, T. Shige, D. E. Laughlin, and J.-G. Zhu, Suppression of low-temperature ferromagnetic phase in ultrathin FeRh films, J. Appl. Phys. **113**, 123909 (2013).

[32] M. Castiella, C. Gatel, J. F. Bobo, N. Ratel-Ramond, R. Tan, M. Respaud, and M. J. Casanove, Structural investigation of magnetic FeRh epitaxial films, Mater. Res. Express **2**, 086401 (2015).

[33] F. Pressacco, V. Uhlíř, M. Gatti, A. Bendounan, E. E. Fullerton, and F. Sirotti, Stable room-temperature ferromagnetic phase at the FeRh(100) surface, Sci. Rep. **6**, 22383 (2016).

[34] C. Gatel, B. Warot-Fonrose, N. Biziere, L. Rodríguez, D. Reyes, R. Cours, M. Castiella, and M. J. Casanove, Inhomogeneous spatial distribution of the magnetic transition in an iron-rhodium thin film, Nat. Commun. **8**, 15703 (2017).

[35] M. G. Loving, R. Barua, C. L. Graët, C. J. Kinane, D. Heiman, S. Langridge, C. H. Marrows, and L. H. Lewis, Strain-tuning of the magnetocaloric transition temperature in model FeRh films, J. Phys. D **51**, 024003 (2018).

[36] I. Suzuki, T. Koike, M. Itoh, T. Taniyama, and T. Sato, Stability of ferromagnetic state of epitaxially grown ordered FeRh thin films, J. Appl. Phys. **105**, 07E501 (2009).

[37] R. Fan, C. J. Kinane, T. R. Charlton, R. Dorner, M. Ali, M. A. de Vries, R. M. D. Brydson, C. H. Marrows, B. J. Hickey, D. A. Arena, B. K. Tanner, G. Nisbet, and S. Langridge, Ferromagnetism at the interfaces of antiferromagnetic FeRh epilayers, Phys. Rev. B **82**, 184418 (2010).

[38] Y. Liu, L. C. Phillips, R. Mattana, M. Bibes, A. Barthélémy, and B. Dkhil, Large reversible caloric effect in FeRh thin films via a dual-stimulus multicaloric cycle, Nat. Commun. **7**, 11614 (2016).

[39] S. P. Bennett, A. T. Wong, A. Glavic, A. Herklotz, C. Urban, I. Valmianski, M. D. Biegalski, H. M. Christen, T. Z. Ward, and V. Lauter, Giant controllable magnetization changes induced by structural phase transitions in a metamagnetic artificial multiferroic, Scientific Reports **6**, 22708 (2016).

[40] Y. Xie, Q. Zhan, T. Shang, H. Yang, B. Wang, J. Tang, and R.-W. Li, Effect of epitaxial strain and lattice mismatch on magnetic and transport behaviors in metamagnetic FeRh thin films, AIP Adv. **7**, 056314 (2017).

[41] J. Chen, J. Ma, Y. Zhang, S. Bao, L. Wu, C. Liu, and C.-W. Nan, Strain modulated ferromagnetic to antiferromagnetic transition in FeRh/$BaTiO_3$ (001) heterostructures, J. Appl. Phys. **121**, 194101 (2017).

[42] C. W. Barton, T. A. Ostler, D. Huskisson, C. J. Kinane, S. J. Haigh, G. Hrkac, and T. Thomson, Substrate induced strain field in ferh epilayers grown on single crystal MgO(001) substrates, Sci. Rep. **7**, 44397 (2017).

[43] A. B. Mei, Y. Tang, J. L. Grab, J. Schubert, D. C. Ralph, and D. G. Schlom, Structural, magnetic, and transport properties of $Fe_{1-x}Rh_x$/MgO(001) films grown by molecular-beam epitaxy, Appl. Phys. Lett. **113**, 082403 (2018).

[44] H. Y. Y. Ko, T. Suzuki, N. N. Phuoc, and J. Cao, Fabrication and characterization of FeRh nanoparticles, J. Appl. Phys. **103**, 07D508 (2008).

[45] M. Loving, F. Jimenez-Villacorta, B. Kaeswurm, D. A. Arena, C. H. Marrows, and L. H. Lewis, Structural evidence for stabilized ferromagnetism in epitaxial FeRh nanoislands, J. Phys. D **46**, 162002 (2013).

[46] P. Ziogas, A. B. Bourlinos, P. Chatzopoulou, G. P. Dimitrakopulos, T. Kehagias, A. Markou, and A. P. Douvalis, Intriguing prospects of a novel magnetic nanohybrid material: Ferromagnetic FeRh nanoparticles grown on nanodiamonds, Metals **12**, 1355 (2022).

[47] A. Hillion, A. Cavallin, S. Vlaic, A. Tamion, F. Tournus, G. Khadra, J. Dreiser, C. Piamonteze, F. Nolting, S. Rusponi, K. Sato, T. J. Konno, O. Proux, V. Dupuis, and H. Brune, Low temperature ferromagnetism in chemically ordered FeRh nanocrystals, Phys. Rev. Lett. **110**, 087207 (2013).

[48] V. Papaefthimiou, F. Tournus, A. Hillion, G. Khadra, D. Teschner, A. Knop-Gericke, V. Dupuis, and S. Zafeiratos, Mixing patterns and redox properties of iron-based alloy nanoparticles under oxidation and reduction conditions, Chem. Mater. **26**, 1553 (2014).

[49] M. Liu, P. Benzo, H. Tang, M. Castiella, B. Warot-Fonrose, N. Tarrat, C. Gatel, M. Respaud, J. Morillo, and M. J. Casanove, Magnetism and morphology in faceted B2-ordered FeRh nanoparticles, Europhys. Lett. **116**, 27006 (2016).

[50] G. Herrera, A. Robert, V. Dupuis, N. Blanchard, O. Boisron, C. Albin, L. Bardotti, Damien Le Roy, F. Tournus, and A. Tamion, Chemical and magnetic order in mass-selected large FeRh nanomagnets embedded in a carbon matrix, Eur. Phys. J. Appl. Phys. **97**, 32 (2022).

[51] L. Motyčková, J. A. Arregi, M. Staňo, S. Průša, K. Částková, and V. Uhlíř, Preserving metamagnetism in self-assembled FeRh nanomagnets, ACS Appl. Mater. Interfaces **15**, 8653 (2023).

[52] See Supplemental Material at http://link.aps.org/supplemental/10.1103/PhysRevB.109.245410 for additional characterization of the BTO thin film, and additional x-ray diffraction/absorption measurements.

[53] A. Barbier, C. Mocuta, D. Stanescu, P. Jegou, N. Jedrecy, and H. Magnan, Surface composition of $BaTiO_3/SrTiO_3$(001) films grown by atomic oxygen plasma assisted molecular beam epitaxy, J. Appl. Phys. **112**, 114116 (2012).

[54] G. Niu, B. Gautier, S. Yin, G. Saint-Girons, P. Lecoeur, V. Pillard, G. Hollinger, and B. Vilquin, Molecular beam epitaxy growth of $BaTiO_3$ thin films and crucial impact of oxygen content conditions on the electrical characteristics, Thin Solid Films **520**, 4595 (2012).

[55] F. Tournus, N. Blanc, A. Tamion, M. Hillenkamp, and V. Dupuis, Synthesis and magnetic properties of size-selected CoPt nanoparticles, J. Magn. Magn. Mater. **323**, 1868 (2011).

[56] V. Dupuis, G. Khadra, A. Hillion, A. Tamion, J. Tuaillon-Combes, L. Bardotti, and F. Tournus, Intrinsic magnetic properties of bimetallic nanoparticles elaborated by cluster beam deposition, Phys. Chem. Chem. Phys. **17**, 27996 (2015).

[57] V. Dupuis, A. Robert, A. Hillion, G. Khadra, N. Blanc, D. L. Roy, F. Tournus, C. Albin, O. Boisron, and A. Tamion, Cubic chemically ordered FeRh and FeCo nanomagnets prepared by mass-selected low-energy cluster-beam deposition: a comparative study, Beilstein J. Nanotechnol. **7**, 1850 (2016).

[58] V. Dupuis, A. Hillion, A. Robert, O. Loiselet, G. Khadra, P. Capiod, C. Albin, O. Boisron, D. Le Roy, L. Bardotti, F. Tournus, and A. Tamion, Bottom-up strategies for the assembling of magnetic systems using nanoclusters, J. Nanopart. Res. **20**, 128 (2018).

[59] R. Alayan, L. Arnaud, A. Bourgey, M. Broyer, E. Cottancin, J. R. Huntzinger, J. Lermé, J. L. Vialle, M. Pellarin, and G. Guiraud, Application of a static quadrupole deviator to the deposition of size-selected cluster ions from a laser vaporization source, Rev. Sci. Instrum. **75**, 2461 (2004).

[60] F. Tournus, Random nanoparticle deposition: Inter-particle distances in 2D, 3D, and multilayer samples, J. Nanopart. Res. **13**, 5211 (2011).

[61] F. Tournus, Multimer formation for two-dimensional random nanoparticle deposition, Phys. Rev. E **84**, 011612 (2011).

[62] Note that in addition to the main peak corresponding to the incident particles (monomers), a second peak corresponds to particles in contact (i.e., dimers) simply due to the random nature of particle deposition [61].

[63] G. Renaud, R. Lazzari, and F. Leroy, Probing surface and interface morphology with grazing incidence small angle x-ray scattering, Surf. Sci. Rep. **64**, 255 (2009).

[64] S. Linas, F. Jean, T. Zhou, C. Albin, G. Renaud, L. Bardotti, and F. Tournus, Moiré induced organization of size-selected Pt clusters soft landed on epitaxial graphene, Sci. Rep. **5**, 13053 (2015).

[65] R. Lazzari, *IsGISAXS:* a program for grazing-incidence small-angle x-ray scattering analysis of supported islands, J. Appl. Crystallogr. **35**, 406 (2002).

[66] The usual h, k, l index notation is used to characterize the diffraction wave-vector (taking the STO lattice as reference, thus using relative lattice units or simply $Å^{-1}$), with the l direction normal to the surface (which is then a (001) plane). We also see the good expitaxy of BTO over the STO single crystal.

[67] This is a rough estimate since we use the simple formula $D_{\text{crystal}} = 6.96/\Delta q$ valid for randomly oriented (powder) spherical particles with a single diameter D. A modified coefficient (as 2π for instance) would however keep the same order of magnitude for the particle size and thus would not change the discussion.

[68] B. D. Cullity and S. R. Stock, *Elements of X-Ray Diffraction*, 3rd ed. (Prentice-Hall Inc., Upper Saddle River, NJ, 2001), pp. 96–102.

[69] Q. Fu and T. Wagner, Interaction of nanostructured metal overlayers with oxide surfaces, Surf. Sci. Rep. **62**, 431 (2007).

[70] Having [110] and [200] directions of FeRh fixed in particular azimuth in the surface planes, then the [001] direction is necessarily perpendicular to the surface and the epitaxy relationship is fully defined.

[71] S. Roobol, W. Onderwaater, J. Drnec, R. Felici, and J. Frenken, *BINoculars*: data reduction and analysis software for

two-dimensional detectors in surface X-ray diffraction, J. Appl. Crystallogr. **48**, 1324 (2015).

[72] It would give a high intensity, both for $\{110\}_{\mathrm{FeRh}}$ and $\{200\}_{\mathrm{FeRh}}$, for directions 9.74° appart from the $\langle h00\rangle_{\mathrm{BTO}}$ and $\langle hh0\rangle_{\mathrm{BTO}}$ azimuths, which is not observed.

[73] J. Olander, R. Lazzari, J. Jupille, B. Mangili, J. Goniakowski, and G. Renaud, Size- and temperature-dependent epitaxy for a strong film-substrate mismatch: The case of Pt/MgO(001), Phys. Rev. B **76**, 075409 (2007).

[74] G. Saint-Girons, C. Priester, P. Regreny, G. Patriarche, L. Largeau, V. Favre-Nicolin, G. Xu, Y. Robach, M. Gendry, and G. Hollinger, Spontaneous compliance of the InP/$SrTiO_3$ heterointerface, Appl. Phys. Lett. **92**, 241907 (2008).

[75] R. Lazzari, G. Renaud, J. Jupille, and F. Leroy, Self-similarity during growth of the Au/TiO_2(110) model catalyst as seen by the scattering of x-rays at grazing-angle incidence, Phys. Rev. B **76**, 125412 (2007).

[76] P. Ohresser, E. Otero, F. Choueikani, K. Chen, S. Stanescu, F. Deschamps, T. Moreno, F. Polack, B. Lagarde, J.-P. Daguerre, F. Marteau, F. Scheurer, L. Joly, J.-P. Kappler, B. Muller, O. Bunau, and P. Sainctavit, DEIMOS: A beamline dedicated to dichroism measurements in the 350–2500 eV energy range, Rev. Sci. Instrum. **85**, 013106 (2014).

[77] G. Radaelli, D. Petti, E. Plekhanov, I. Fina, P. Torelli, B. R. Salles, M. Cantoni, C. Rinaldi, D. Gutiérrez, G. Panaccione, M. Varela, S. Picozzi, J. Fontcuberta, and R. Bertacco, Electric control of magnetism at the Fe/$BaTiO_3$ interface, Nat. Commun. **5**, 3404 (2014).

[78] A. Tamion, E. Bonet, F. Tournus, C. Raufast, A. Hillion, O. Gaier, and V. Dupuis, Efficient hysteresis loop simulations of nanoparticle assemblies beyond the uniaxial anisotropy, Phys. Rev. B **85**, 134430 (2012).

[79] G. Barcaro, L. Sementa, F. R. Negreiros, R. Ferrando, and A. Fortunelli, Interface effects on the magnetism of CoPt-supported nanostructures, Nano Lett. **11**, 5542 (2011).

Correction: A second affiliation was inadvertently added to the thirteenth author and has been fixed.